

Porous Biomass Carbon Derived from Peanut Shells as Electrode Materials with Enhanced Electrochemical Performance for Supercapacitors

Zuoan Xiao¹, Wenwen Chen¹, Ke Liu², Ping Cui¹, Dan Zhan^{1,2,*}

¹ Department of Chemical Engineering, Hubei University of Arts and Science, Xiangyang, 441053, P. R. China

² Hubei Key Laboratory of Low Dimensional Optoelectronic Materials and Devices, Xiangyang, 441053, P. R. China

*E-mail: dan_zhan@126.com

Received: 8 February 2018 / Accepted: 30 March 2018 / Published: 10 May 2018

A hierarchical porous carbon with high surface area derived from peanut shells was synthesized via a simple, valid and economical route involving hydrothermal treatment, ZnCl₂ activation and pyrolysis. The products were characterized by XRD, SEM, Raman and Brunauer Emmett-Teller (BET) tests. The electrochemical performance was explored by cyclic voltammetry, galvanostatic charge-discharge and electrochemical impedance measurements. It was found that the peanut shell-derived carbon electrode materials in supercapacitors exhibited high capacitance (340 F g⁻¹), excellent rate performance (54.7% capacitance retention from 0.25 A g⁻¹ to 50 A g⁻¹) and outstanding cycle stability (capacitance decay of 4.7% after 10000 cycles at 1 A g⁻¹), which benefit from the unique hierarchical structure. The excellent electrochemical performance endows the peanut shell-derived carbon with promising prospects for high performance supercapacitors.

Keywords: peanut shell; porous carbon; ZnCl₂ activation; supercapacitors; electrochemical performance.

1. INTRODUCTION

With the increasing global awareness of environmental protection and growing demand for clean energy, supercapacitors are considered promising energy storage devices due to the merits of rapid recharging, long cycling tolerance and high power density [1, 2]. The electrode material of supercapacitor is the major factor to influence the electrochemical performance and has attracted intensive attention. Among those electrode materials, including carbon materials, metal oxides and conductive polymers, carbon materials are regarded as the most promising candidate owing to the

excellent structure elasticity, good conductivity and resource abundance [3, 4]. For porous carbon materials, the pore structure provides a high accessible surface area, leading to a high capacitance and a high energy density, which plays an essential role in high energy storage. Additionally, the interconnected macropores and mesopores facilitate fast ion transport through supplying ion-buffering reservoirs and ion-transport routes, which ensure the high rate capability and high power density [5-7]. Generally, porous carbon materials are prepared from costly and non-renewable coal and petroleum via a template, involving highly toxic chemicals and complicated, expensive and time-consuming procedures [5], which limits their commercial application. Therefore, there is an urgent demand to design porous carbon via a renewable route. Recently, some novel strategies for the synthesis of hierarchical porous carbon were proposed, such as co-assembly and self-templating [8-10].

Meanwhile, biomass material not only contains abundant carbon, existing as cellulose, lignin and hemicelluloses, but also usually exhibits a unique hierarchical porous structure. Moreover, rational utilization of biomass is conducive to environmental protection and sustainable development. Therefore, the utilization of biomass to produce hierarchical porous carbon materials has become more and more attractive, especially for energy storage [11-14]. Until now, various kinds of biomass have been transformed into porous carbon materials, such as corncob and straw [15], rice husks [9], as well as batata leaves and stalks [16]. Porous activated carbon derived from peanut shells was used widely not only in the field of environmental protection as an efficient adsorbent to remove heavy metal ions and organic dyestuff in waste water [17-18] but also in power sources such as lithium-/sodium-ion batteries and capacitors [19-21]. Lv et al. prepared peanut shell-derived porous hard carbon using KOH activation and a pyrolysis process, which delivered a retained capacity of 474 mA h g⁻¹ after 400 cycles at 1 A g⁻¹ as anode materials for a lithium-ion battery and 193 mA h g⁻¹ after 400 cycles at 0.25 A g⁻¹ for a sodium-ion battery [19]. Wu et al. synthesized activated carbon from peanut shells by KOH activation under microwave heating, exhibiting excellent electrochemical performance used as electrode materials for electrochemical capacitors [20]. Guo et al. prepared microporous carbon materials directly by the carbonization of peanut shells with NaOH pretreatment and investigated their electrochemical performance as electrode materials for supercapacitors. It was found that the peanut shell-derived carbon electrode showed a specific capacitance as high as 378 F g⁻¹ and good cycle stability [21]. Yin et al. prepared capacitive carbons by a molten salt Na₂CO₃-K₂CO₃ carbonization process using various waste biomasses, including straw, peanut husks, rice husks, pomelo peels, corn cores and chestnut hulls. Among those, the peanut husk-derived carbon exhibited a high specific capacitance of 160 F g⁻¹, and retained 95% after 10000 cycles [22].

Herein, hierarchical porous carbon with a large surface area (1549 m² g⁻¹) derived from peanut shells was synthesized via a simple, efficient and economical route involving hydrothermal treatment, ZnCl₂ activation and pyrolysis. The electrochemical performance was explored by cyclic voltammetry (CV), galvanostatic charge-discharge (GCD) and electrochemical impedance measurements (EIS). Benefiting from the unique hierarchical structure, the peanut shell-derived carbon demonstrated high capacitance and excellent rate performance as electrode materials for supercapacitors. These as-obtained biomass carbon materials would be favourable for supercapacitors with high performance in view of the combined merits of both excellent electrochemical performance and low-cost production.

2. EXPERIMENTAL

2.1 Material synthesis

The peanut shells in this work were obtained from a local market (Xiangyang, China). All other chemical reagents used in this work were of analytical grade and used directly. Deionized water was used throughout. The peanut shells were first washed by water and ethanol several times successively and then dried in air at 120 °C overnight. The dried peanut shells were crushed to powder with 200 meshes. Subsequently, the peanut shell powder was impregnated into 2 mol L⁻¹ zinc chloride solution at a mass ratio of 1:1.5 under continuous stirring. Then, the above mixture was transferred into a 90 mL Teflon-lined stainless autoclave and heated at 120 °C for 10 h. After cooling to ambient temperature naturally, the as-treated mixture was calcined in a tube furnace at 550 °C for 2 h under argon atmosphere with a heating rate of 5 °C min⁻¹ and cooled naturally to room temperature. The resultant products were washed with 0.1 mol L⁻¹ hydrochloric acid solution and deionized water several times, respectively, and then further dried at 120 °C in air overnight. The schematic diagram of the preparation procedure is shown in **Fig. 1**. For convenience, the as-obtained sample is labelled as a-PnC, and another sample obtained from direct calcination of peanut shell powder is labelled as PnC for comparison.

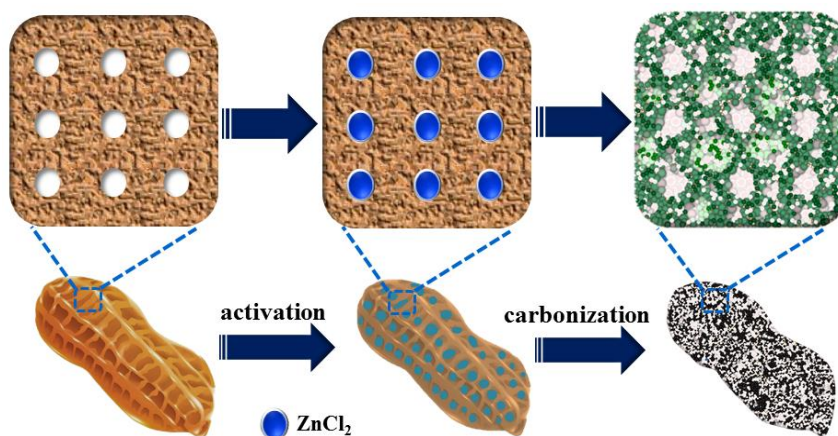


Figure 1. Schematic diagram for the preparation of porous carbon from peanut shell with ZnCl₂ activation (a-PnC)

2.2 Material characterization

The thermogravimetric analysis (TG) of pyrolysis process was carried out on a thermogravimetric instrument (Labsys Evo, French). The phase composition and crystal structure of the obtained carbon were analysed on an X-ray diffractometer (XRD, Bruker D8 Advance, German) with Cu K_α radiation ($\lambda = 0.15418$ nm) under a current of 40 mA and a voltage of 40 kV. The morphology of the samples was surveyed by a field-emission scanning electron microscope (SEM, NOVA NANO 230, Japan). The chemical component analysis was carried out using an EDAX energy

dispersive spectroscopy (EDS) system interfaced with the FESEM. Raman spectra were obtained using the 523 nm line of an Ar-ion laser as the excitation source of a Raman microscope (Renishaw, invia, England). The Brunauer Emmett-Teller (BET) tests were performed by N₂ isothermal adsorption using a compact specific surface area and pore size analyser (Belsorp-Mini-II, Japan). The pore size distribution (PSD) was calculated by the Barret-Joyer Halenda (BJH) model according to nitrogen adsorption data.

2.3 Electrochemical measurement

The electrochemical properties of the samples were measured using a three-electrode system or two-electrode system in 1 mol L⁻¹ H₂SO₄ aqueous solution under ambient conditions. The carbon electrode film used as the working electrode (1 cm², 10 mg) was composed of the as-obtained carbon (80 wt %), acetylene (10 wt %) black and Poly(tetrafluoroethylene) (PTFE, 10 wt %) binder, which was pressed on a stainless steel grid. For the three-electrode system, the counter and reference electrodes were a platinum plate and an Hg/Hg₂SO₄ electrode, respectively. The two-electrode system is assembled using two equal as-obtained carbon electrodes. The cyclic voltammetry (CV) and electrochemical impedance (EIS) measurements were performed in a three-electrode system, and the galvanostatic charge-discharge (GCD) tests were conducted in a two-electrode system. CV and GCD tests were carried out on an electrochemical workstation (CHI 660 a, China). EIS measurements were conducted on another electrochemical workstation (Autolab PGSTAT302N, Switzerland) at open circuit potential in a sweeping frequency range of 0.01-10 kHz by applying an AC signal of 5 mV in amplitude throughout the test. The specific capacitance, the stored specific energy and the power density were calculated according to the equations in a previous report [16].

3. RESULTS AND DISCUSSION

3.1 Structure and morphology characterization

It is known that biomass, including peanut shells, is mainly composed of cellulose, hemicelluloses and lignin, which usually partially become volatile gases (such as CO, H₂, CH₄, C₂H₄) and residue mainly composed of carbon under a sufficiently high temperature [18, 23]. To determine the proper pyrolysis temperature, TG and differential thermogravimetric (DTG) measurement were employed to investigate the pyrolysis process of peanut shells in a N₂ atmosphere. As can be seen from Fig. 2a, the main weight loss of approximately 81% occurred in the temperature range of 230~500 °C, associated with the release of water or incondensable gas during the pyrolysis process. When heated to a temperature above 500 °C, the sample maintained a constant weight, suggesting the termination of the pyrolysis process. Therefore, 550 °C was considered the proper pyrolysis temperature to prepare activated carbon derived from peanut shells in this work.

Fig. 2b shows the XRD pattern of the as-obtained carbon. Both of the samples demonstrated a similar pattern corresponding to amorphous carbon. The peak at 2 θ=23° was ascribed to the (002)

crystal plane, while the peak at $2\theta=43^\circ$ corresponds to the (100) plane. Both of the peaks are broad and weak, suggesting that amorphous carbon was present in the samples. The (002) crystal plane reflects parallel stacked grapheme sheets and small domains of coherence, while the (100) crystal plane implies a typical honeycomb structure formed by sp^2 hybridized carbons [24]. In contrast to the carbon obtained without $ZnCl_2$ activation (PnC), the intensity of the carbon with $ZnCl_2$ activation (a-PnC) is lower, indicating the lower degree of graphitization.

The Raman spectra of the two samples are shown in Fig. 2c. Two broad peaks are observed at 1320 cm^{-1} and 1590 cm^{-1} , corresponding to D-band and G-band, respectively. Generally, the D-band stands for sp^3 hybridized carbon with the chaotic state, and the G-band represents the sp^2 hybridized carbon with a graphite structure [25]. The intensity ratio I_D/I_G was applied to evaluate the disorder degree of the bio-carbons formed. A higher I_D/I_G value represents higher content of disordered carbon sheets [15]. As Figure 2c shows, the calculated peak intensity ratio value (I_D/I_G) of a-PnC (0.89) is larger than that of PnC (0.84), indicating that the peanut shell-derived carbon with $ZnCl_2$ activation contained defects presenting a much more disordered state, agreeing with the results of XRD.

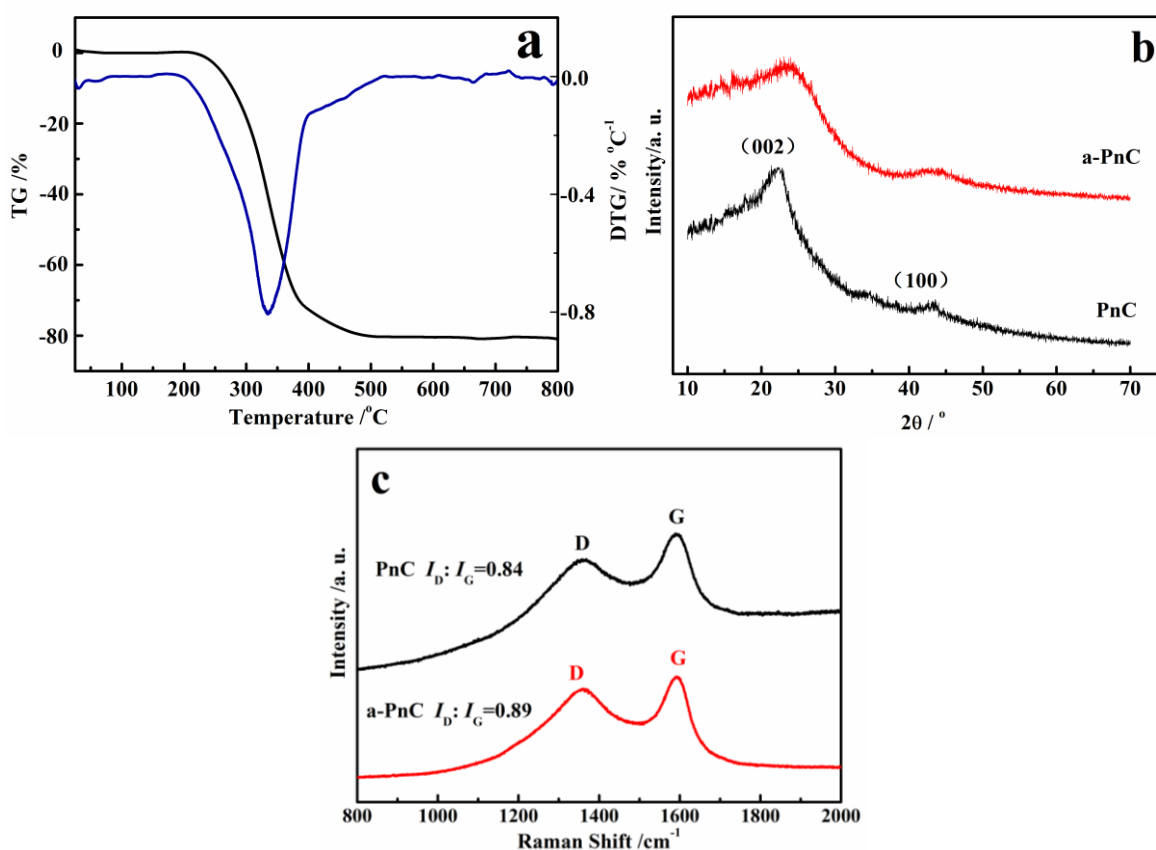


Figure 2. (a) TG and DTG curves of the peanut shell recorded in N_2 atmosphere at a heating rate of 10 K min^{-1} ; (b) XRD patterns; (c) Raman spectra of PnC and a-PnC.

The morphology and the chemical ingredients of the samples were characterized by SEM, EDS and element mapping, respectively. Fig. 3a, b, c, and d show SEM images of the samples. Fig. 3a

demonstrates that the PnC sample mainly appears as a blocky structure with some pores; even in the magnified SEM image (Fig. 3c) the smooth surface with a large area was clearly observed. However, as observed in Figure 3b and 3d, a-PnC shows a quite distinct multilevel pore structure. In particular, in Fig. 3d, some macropores with diameters of approximately 4 μm were easily found, and also quite a lot of pores with different sizes, including micropores and mesopores, were observed in the magnified image of the red rectangle area (inset of Fig. 3d). It was reported that ZnCl_2 has the effect of catalytic dehydroxylation and dehydration during heating, which makes hydrogen and oxygen in the raw material release in the form of vapour, resulting in the porous structure of the product [26]. Suat Uçar et al. reported that gasified ZnCl_2 at high temperature entered into the biomass and acted as a framework. Carbon polymer deposited on the framework after carbonization. When ZnCl_2 was washed away using acid, porous carbon with high specific surface area was produced [27]. Based on the previous reports, it is not difficult to understand here that the carbon obtained using ZnCl_2 activation (a-PnC) has a richer porous structure than the carbon sample (PnC) obtained through direct calcination without ZnCl_2 activation process. From the EDS spectrum in Fig. 3e for a-PnC sample, the dominant component of the sample is carbon, and hardly any other elements were found. Fig. 3f is the element mapping corresponding to the SEM image in the inset of Figure 3e for the as-obtained carbon. It shows that the sample mainly contained carbon, agreeing with the above EDS result.

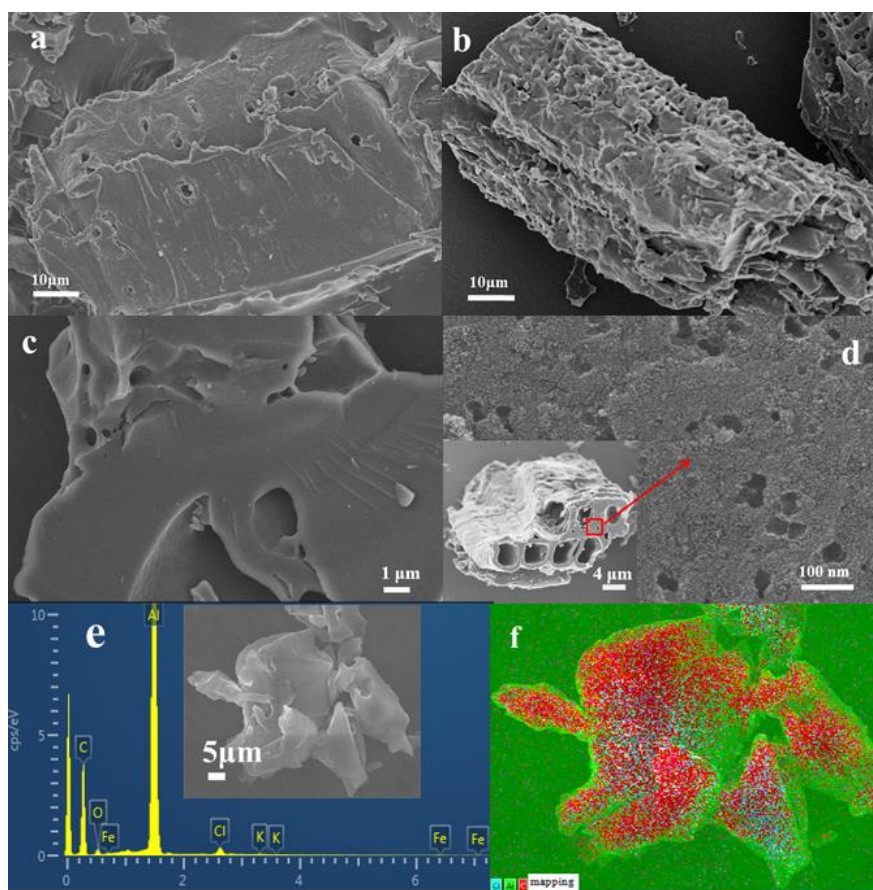


Figure 3. The SEM images of the PnC (a, c), a-PnC (b, d), the inset of (e); the EDS spectrum (e) and mapping (f) corresponding to the inset of (e) of the a-PnC.

Nitrogen adsorption-desorption isotherms were employed to analyse the pore structure of PnC and a-PnC depicted in Fig. 4. The nitrogen adsorption-desorption isotherms of the two samples exhibited a hybrid I/IV type adsorption isotherms, suggesting the coexistence of micro-, meso- and macropores in a-PnC and PnC [28]. A strong N_2 adsorption occurred at a relatively low pressure below $0.1 p/p^0$, suggesting the presence of micropores. The hysteresis loops at $0.4-0.8 p/p^0$ between the adsorption and desorption resulting from the capillary condensation imply the existence of mesopores, and the hysteresis loops of the a-PnC look more distinct. Additionally, a slightly steep adsorption at the relative pressure of $0.8-1.0$ was observed in the curves for a-PnC, suggesting the presence of macropores. These results agree with the PSD (Fig. 4b). The PSD curves show that both the PnC and a-PnC contain micropores and mesopores. The pore sizes of a-PnC mainly were centred at approximately 1.89 nm and 4.21 nm, while the PnC had pore sizes centred at approximately 1.69 nm and 3.47 nm. The larger average pore size of a-PnC can speed up the electron and ionic transport as well as increase the surface area. Calculated by the BET model, the specific surface area of a-PnC was $1549 \text{ m}^2 \text{ g}^{-1}$, much larger than that of PnC ($1069 \text{ m}^2 \text{ g}^{-1}$). Such a large specific surface area can increase the contact region between the electrode and electrolyte for the accumulation of ions and enhance the capacitance performance.

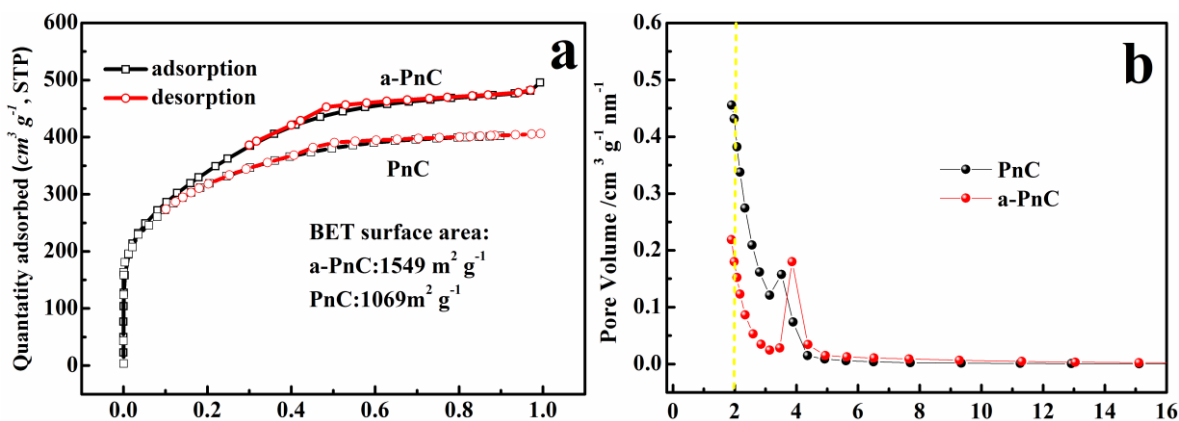


Figure 4. (a) Nitrogen adsorption-desorption isotherms and (b) Pore size distribution curves of PnC and a-PnC

3.2 Electrochemical properties

The electrochemical properties of the peanut shell-derived carbon materials were explored in $1 \text{ mol L}^{-1} \text{ H}_2\text{SO}_4$ aqueous electrolyte. CV measurements at 10 mV s^{-1} were used to estimate the specific capacitance of the as-obtained carbon with/without ZnCl_2 activation. The results were shown as CV curves in Fig. 5a. Apparently, the CV curve of the a-PnC sample shows a much more similar rectangle shape than the PnC sample, indicating a much better capacitive property. Fig. 5b shows the CV profiles with various scanning rates between -0.2 and 0.8 V for a-PnC. The quasi-rectangle shape can be maintained even at a high current density of 50 mV s^{-1} , suggesting the typical stable double layer capacitor and quick efficient charge transfer and excellent capacitive behaviour of the material [29].

Fig. 5c displayed the galvanostatic charge-discharge curves of the two carbon samples at a current density of 0.5 A g^{-1} . The approximately symmetric characteristic of the curves revealed the good reversibility of electron conductivity for both of the samples. The specific capacitances are 333 and 221 F g^{-1} , respectively, indicating that the as-obtained carbon delivered a higher capacitance. The excellent capacitive performance of a-PnC is mainly due to the higher specific surface area, which can provide more contact area between electrode and electrolyte for the accumulation of ions. All the galvanostatic charge-discharge curves (Fig. 5d) for a-PnC at different current densities display a symmetric triangular shape without an obvious IR drop, implying the small internal resistance and good capacitive performance of the material. The specific capacitance values are calculated to be 340, 333, 325, 304 F g^{-1} under current densities of 0.25, 0.5, 1, 2 A g^{-1} , respectively. With the increase of current density, the specific capacitances decreased gradually, possibly due to insufficient time for electrolyte diffusion into all the pores under a high current density [30]. A comparison with the literature data on the electrochemical capacitance of biomass-derived carbons is listed in Table 1, suggesting the excellent electrochemical capacitive performance of our as-obtained carbon.

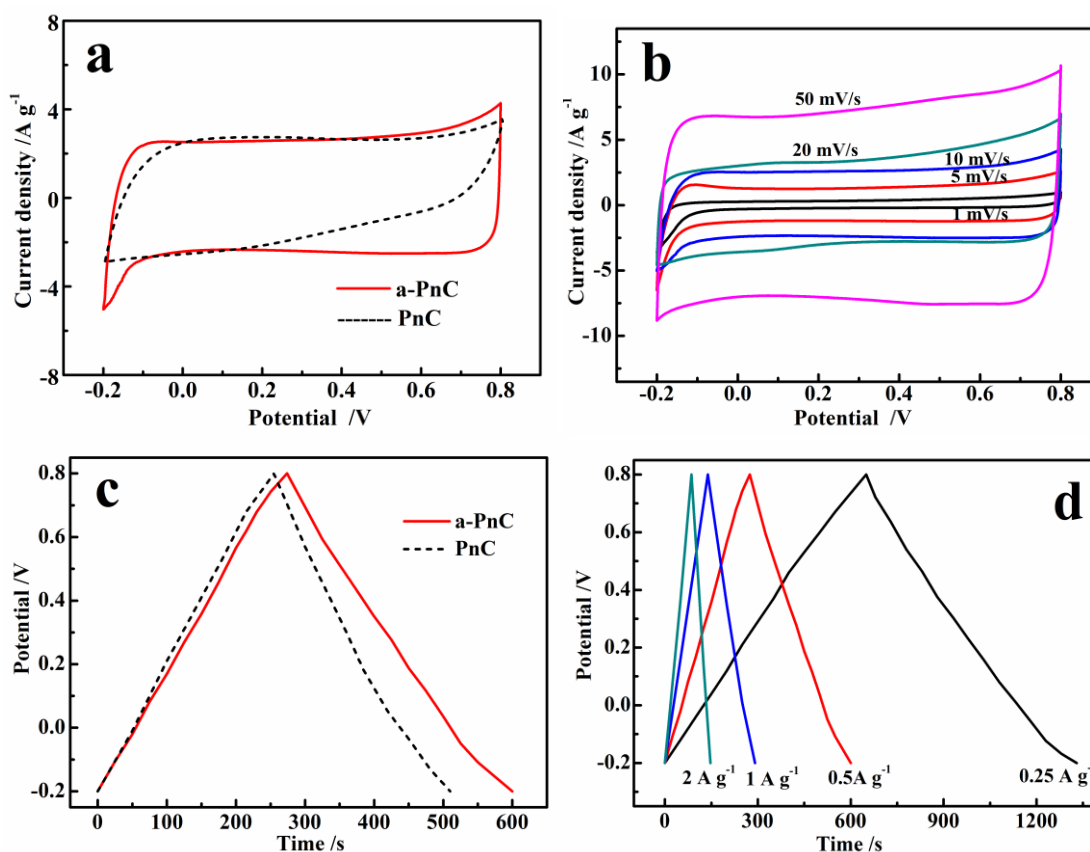


Figure 5. (a) CV curves at a scan rate of 10 mV s^{-1} for PnC and a-PnC; (b) CV curves at different scan rates for a-PnC; (c) galvanostatic charge-discharge curves at a current density of 0.5 A g^{-1} for PnC and a-PnC; (d) galvanostatic charge-discharge curves at different current density for a-PnC.

Table 1. Comparison of capacitive performances of biomass-derived carbons

Biomass precursor	Electrolyte	Specific capacity (F g ⁻¹)	Reference
Rice husks	6 M KOH	278	9
Cotton	1 M H ₂ SO ₄	252	13
Batata leaves	1 M H ₂ SO ₄	532.5	16
Peanut shells	6M KOH	233	21
Peanut shells	1 M H ₂ SO ₄	148	22
Rice risk	6 M KOH	245	26
Willow catkins	1 M H ₂ SO ₄	340	29
Melaleuca barks	1 M H ₂ SO ₄	233	30
Peanut shells	1 M H ₂ SO ₄	340	This work

Fig. 6a shows the variation of the specific capacitance at different current densities for PnC and a-PnC. It is clear that a-PnC exhibited higher capacitance than PnC even at a high current density of 50 A g⁻¹. Moreover, the a-PnC still has 54.7% capacitance retention from 0.25 A g⁻¹ to 50 A g⁻¹, exhibiting an excellent rate capability. That is mainly ascribed to the hierarchically porous structure providing favourable diffusion routes for the electrolyte. Considering that cycling stability is an important electrochemical feature for supercapacitors, the galvanostatic charge-discharge of the a-PnC electrode was performed for 10000 cycles at 1 A g⁻¹. As Fig. 6b shows, the capacitance of a-PnC decreased by only 4.7% after 10000 cycles, indicating its good stability as a supercapacitor electrode material. To further comprehend the electrochemical behaviour of the carbons, Nyquist plots of PnC and a-PnC are presented in Fig. 6c. At low frequency, the straight line is approximately perpendicular to the real axis, suggesting a good conductivity of charge and excellent electrochemical capacitance performance, which agrees with the analysis of the CV measurement [31]. At high frequency, a semicircle on the impedance of each sample was observed. The diameter of the semicircle represents the interfacial charge-transfer resistance (R_{ct}), which is usually the limiting factor of the power density of supercapacitors [32]. A smaller semicircle indicated a lower charge-transfer resistance. As shown in Fig. 6c, the a-PnC exhibited smaller R_{ct} (0.65 Ω) than PnC (0.78 Ω), indicating better conductivity. The solution resistance (R_s) values, determined from the intercept at the real axis (Z') in the high frequency region, are 0.47 Ω for a-PnC and 0.72Ω for PnC. The considerably lower R_s of a-PnC is mainly because of the lower contact resistance between the ion and a-PnC, which has a hierarchical porous structure. These results confirm the excellent electrochemical capacitive properties of the a-PnC electrode due to the unique porous structure and high specific surface area facilitating rapid electron and ion transport, as previously mentioned [33].

To evaluate the energy density (E) and power density (P) of the PnC and a-PnC electrodes, a Ragone plot is presented in Fig. 6d. E and P are calculated by the equations $E = CV^2/2$ and $P = E/t$ (where C, V and t are specific capacitance, potential range and a full discharge time, respectively). The energy density of the two samples decreased slowly with the increase in power density. When the power density of the a-PnC electrode increased from 106.9 to 6250 W kg⁻¹, the energy density decreased from 10.8 to 6.9 Wh kg⁻¹. In contrast, the PnC electrode shows an energy density of 8.5-4.6 Wh kg⁻¹ at 100.6-6562 W kg⁻¹. Obviously, the energy density of the a-PnC electrode is superior to the PnC

electrode. Based on the above results, it can be concluded that the a-PnC electrode is capable of delivering high power without profound loss in energy, indicating a promising application in electrochemical capacitors.

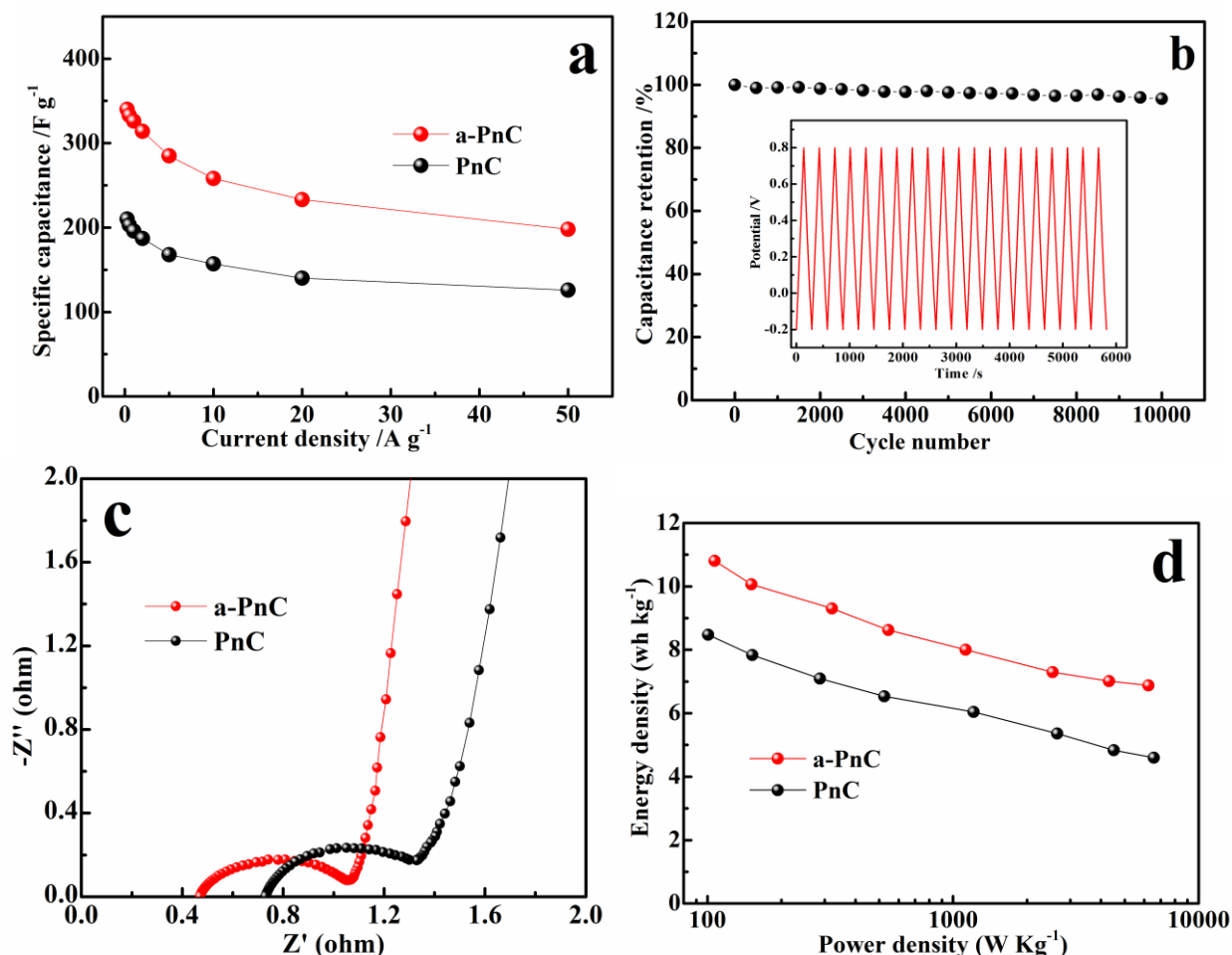


Figure 6. (a) Specific capacitances of the PnC and a-PnC at different current densities; (b) cycle stability of the a-PnC at a current density of 1 $A g^{-1}$, where the inset is the first twenty cycles; (c) Nyquist plots of PnC and a-PnC electrodes; (d) Ragone plot of PnC and a-PnC.

4. CONCLUSIONS

In this work, an effective strategy for the fabrication of hierarchical porous carbon derived from peanut shells was developed through a simple process involving hydrothermal treatment, $ZnCl_2$ activation and pyrolysis. The hierarchical structure consists of micropores, mesopores and macropores with a large specific surface area ($1549 m^2 g^{-1}$), larger than the specific surface area of the carbon derived from direct calcination without $ZnCl_2$ activation ($1069 m^2 g^{-1}$). Such a high specific surface area leads to the excellent capacitive electrochemical performance of the as-obtained carbon as an electrode material for supercapacitors. The specific capacitance was as high as $333 F g^{-1}$ under a current density of $0.5 A g^{-1}$. The a-PnC still showed 54.7% capacitance retention from $0.25 A g^{-1}$ to $50 A g^{-1}$.

A g^{-1} , exhibiting an excellent rate capability. Moreover, the capacitance of a-PnC decreased by only 4.7% after 10000 cycles, implying good stability as electrode materials for supercapacitors. In view of the above simple fabrication route and the excellent capacitive performance, it can be concluded that the peanut shell derived carbon with ZnCl_2 activation as an electrode is qualified for delivering high power, suggesting a promising application in supercapacitors.

ACKNOWLEDGEMENTS

Dr. Ke Fan from Wuhan University of Technology is greatly appreciated for his valuable advice and help. This work was supported by the National Natural Science Foundation of China (grant number 51708191), the Natural Science Foundation of Hubei Province (grant number 2017CFC857), the Petroleum and Chemical Industry Federation Program of China (grant number 20170902), and Teachers' Scientific Research funds of Hubei University of Arts and Science (grant number 2016ZK008).

References

1. N. Devillers, S. Jemei, M. C. Péra, D. Bienaimé and F. Gustin, *J. Power Sources*, 246 (2014) 596.
2. M. Hughes, G. Z. Chen, M. S. P. Shaffer, D. J. F. And A. H. Windle, *Chem. Mater.*, 14 (2016) 1610.
3. F. Béguin, V. Presser, A. Balducci and E. Frackowiak, *Adv. Mater.*, 26 (2014) 2219.
4. Y. Zhu, S. Murali, M. D. Stoller, K. J. Ganesh, W. Cai, P. J. Ferreira, A. Pirkle, R. M. Wallace, K. A. Cychoz, M. Thommes, D. Su, E. A. Stach and R. S. Ruoff, *Science*, 332 (2011) 1537.
5. Q. Wang, J. Yan, Y. Wang, T. Wei, M. Zhang, X. Jing and Z. Fan, *Carbon*, 67 (2014) 119.
6. M. Sevilla and A. B. Fuertes, *Acs Nano*, 8 (2014) 5069.
7. D. Liu, Z. Jia and D. Wang, *Carbon*, 100 (2016) 664.
8. J. Wang, S. Feng, Y. Song, L. Wei, W. Gao, A. A. Elzatahry, D. Aldhayan, Y. Xia and D. Zhao, *Catal. Today*, 243 (2015) 199.
9. D. Liu, W. Zhang, H. Lin, Y. Li, H. Lu and Y. Wang, *RSC Adv.*, 5 (2015) 19294.
10. J. Zhang, D. Yang, W. Li, Y. Gao and H. Li, *Electrochim. Acta*, 130 (2014) 699.
11. Q. Jiang, Z. Zhang, S. Yin, Z. Guo, S. Wang and C. Feng, *Appl. Surf. Sci.*, 379 (2016) 73.
12. J. Wang, P. Nie, B. Ding, X. Hao, S. Dong, H. Dou and X. Zhang, *J. Mater. Chem. A*, 5 (2017) 2411.
13. Y. X. Hao, M. Qian, J. J. Xu, H. Bi and F. Q. Huang, *J. Inorg. Mater.*, 33 (2018) 93.
14. Y. Zhu, G.Y. Xu, X. L. Zhang, S. J. Wang, C. Li and G. X. Wang, *J. Alloy. Compd.*, 695 (2017) 2246.
15. A. Wu, J. Yan, W. Xu and X. Li, *Mater. Lett.*, 173 (2016) 60.
16. X. Wei, Y. Li and S. Gao, *J. Mater. Chem. A*, 5 (2017) 181.
17. S. J. Lee, H. P. Jin, Y. T. Ahn and J. W. Chung, *Water, Air, & Soil Pollution*, 226 (2015) 1.
18. J. Georgin, G. L. Dotto, M. A. Mazutti and E. L. Foletto, *J. Environ. Chem. Eng.*, 4 (2016) 266.
19. W. Lv, F. Wen, J. Xiang, J. Zhao, L. Li, L. Wang, Z. Liu and Y. Tian, *Electrochim. Acta*, 176 (2015) 533.
20. M. B. Wu, R. C. Li, X. J. He, H.B. Zhang, W.B. Sui and M. H. Tan, *New Carbon Mater.*, 30 (2015) 86.
21. P. Z. Guo, Q. Q. Ji, L. L. Zhang, S. Y. Zhao and X. S. Zhao, *Acta Physico-Chim. Sin.*, 27 (2011) 2836.
22. H. Yin, B. Lu, Y. Xu, D. Tang, X. Mao, W. Xiao, D. Wang and A. N. Alshawabkeh, *Environ. Sci. & Technol.*, 48 (2014) 8101.
23. E. M. Rubin and E. M. Rubin, *Nature*, 454 (2008) 841.

24. X. Yu, K. Zhang, N. Tian, A. Qin, L. Liao, R. Du and C. Wei, *Mater. Lett.*, 142 (2015) 193.
25. A.V. Bridgwater, *Biomass & Bioenergy*, 38 (2012) 68.
26. X. He, P. Ling, M. Yu, X. Wang, X. Zhang, M. Zheng, X. He, P. Ling, M. Yu and X. Wang, *Electrochim. Acta*, 105 (2013) 635.
27. S. Uçar, M. Erdem, T. Tay and S. Karagöz, *Appl. Surf. Sci.*, 255 (2009) 8890.
28. M. Thommes, K. Kaneko, A. V. Neimark, J. P. Olivier, F. Rodriguez-Reinoso, J. Rouquerol and K. S. W. Sing, *Pure Appl. Chem.*, 87 (2015) 1051.
29. W. Kai, Z. Ning, S. Lei, Y. Rui, X. Tian, J. Wang, S. Yan, D. Xu, Q. Guo and L. Lang, *Electrochim. Acta*, 166 (2015) 1.
30. Q. P. Luo, L. Huang, X. Gao, Y. Cheng, B. Yao, Z. Hu, J. Wan, X. Xiao and J. Zhou, *Nanotechnology*, 26 (2015) 304004.
31. X. Ma, L. Gan, M. Liu, P. Tripathi, Y. Zhao, Z. Xu, D. Zhu and L. Chen, *J. Mater. Chem. A*, 2 (2014) 8407.
32. W. Xiao, H. Xia, J. Y. H. Fuh and L. Lu, *J. Power Sources*, 193 (2009) 935.
33. J. Liu, X. Wang, J. Gao, Y. Zhang, Q. Lu and M. Liu, *Electrochim. Acta*, 211 (2016) 183.

© 2018 The Authors. Published by ESG (www.electrochemsci.org). This article is an open access article distributed under the terms and conditions of the Creative Commons Attribution license (<http://creativecommons.org/licenses/by/4.0/>).